

# Whole-Body Control with Motion/Force Transmissibility for Parallel-Legged Robot

Jiajun Wang<sup>1</sup>, Gang Han<sup>1</sup>, Xiaozhu Ju<sup>1</sup> and Mingguo Zhao<sup>2</sup>

**Abstract**—Whole-body control (WBC) has been applied to the locomotion of legged robots. However, current WBC methods have not considered the intrinsic features of parallel mechanisms, especially motion/force transmissibility (MFT). In this work, we propose an MFT-enhanced WBC scheme. Introducing MFT into a WBC is challenging due to the nonlinear relationship between MFT indices and the robot configuration. To overcome this challenge, we establish the MFT preferable space of the robot and formulate it as a polyhedron in the joint space at the acceleration level. Then, the WBC employs the polyhedron as a soft constraint. As a result, the robot possesses high-speed and high-acceleration capabilities by satisfying this constraint as well as staying away from its singularity. In contrast with the WBC without considering MFT, our proposed scheme is more robust to external disturbances, e.g., push recovery and uneven terrain locomotion. simulations and experiments on a parallel-legged bipedal robot are provided to demonstrate the performance and robustness of the proposed method.

## I. INTRODUCTION

The parallel mechanism usually has low inertia, high stiffness, and more importantly, it presents the characteristics of high-load capacity, high-speed capability and excellent dexterity. Consequently, many legged robots use the parallel mechanism, e.g., Atrias [1], Cassie [2], Digit [3], Minitaur [4], and Ollie [5].

The common challenges of the legged robot locomotion are the limitations of actuators, the changing unilateral contact constraints and possibly conflicting tasks [6], [7], [8], [9]. As these challenges can be formulated as either convex cost functions or constraints, quadratic programming (QP) based WBCs have been increasingly used to cope with the above challenges [10], [11], [12], [13]. Furthermore, for legs with parallel mechanisms, the QP-based WBC must model the dynamics and kinematics of the closed-loop chains. A standard approach is to manage it by cutting the loops and enforcing holonomic constraints [14], [15], [16]. The above formulations have achieved remarkable performance for parallel-legged robots in many scenarios. However, robots are desired to work in more complex environments. Therefore, recent works introduced more features as either constraints or costs to enhance the robustness of the robots. For example, Kim et al. considered contact reaction force as constraints for better contact transitions [16], and Reher et al. introduced the control Lyapunov functions by modifying the costs and

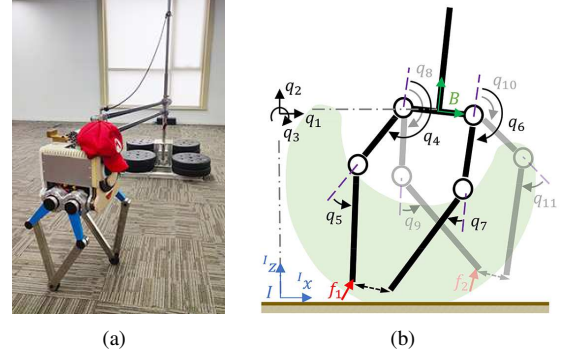


Fig. 1. (a) Parallel-legged bipedal robot. (b) The kinematic scheme of the robot. The dashed double-arrows at ankles represent the closed-loop holonomic constraints, and the light green area indicates the MFT preferable space of the right foot with respect to the floating-base  $B$ .

constraints of QP to render better convergence in the context of tracking outputs [17].

In this work, we introduce MFT as soft inequality constraints to QP-based WBC for the enhancement of dexterity and robustness. Parallel robots usually use multiple closed-loop chains with passive joints to transmit the motion and force from the actuators on one side to the end effector on the other side. Thus, the MFT of parallel mechanisms has significantly influence on the robot's kinematic and dynamic performance, e.g., speed ability, accuracy, acceleration capacity and even power efficiency. Many indices have been proposed to analyze the MFT. Chen et al. proposed the power coefficient to evaluate the MFT for single-loop mechanisms [18]. The local transmission index (LTI) proposed in [19] and [20] evaluates the MFT for multi-loop mechanism. And the LTI can also measure the closeness to the singularity for parallel mechanisms. Then the relationship between the MFT and the dynamic performance was analyzed, and the robot acceleration capacity index (RACI) was consequently proposed for various parameters synchronous optimization [21]. MFT has been commonly used in the parameters optimization design of parallel robots [22]. But it is rarely used in the real-time control since MFT indices have nonlinear relationships with the configurations of the robot. However, for reasons that external disturbances and improper plannings of tasks worsen the MFT, the future tasks performance cannot be guaranteed. Thus, we include MFT constraint in the real-time control to consider the intrinsic feature of parallel-legged robot.

To sum up, we propose an MFT-enhanced WBC scheme for the parallel-legged robot locomotion, namely MFT-WBC.

<sup>1</sup>Jiajun Wang, Gang Han, and Xiaozhu Ju are with Beijing Research Institute of UBTECH Robotics, Beijing, China. {jiajun.wang, gang.han, xiaozhu.ju}@ubtrobot.com

<sup>2</sup>Mingguo Zhao is with the Department of Automation, Tsinghua University, Beijing, China. mgzhao@mail.tsinghua.edu.cn

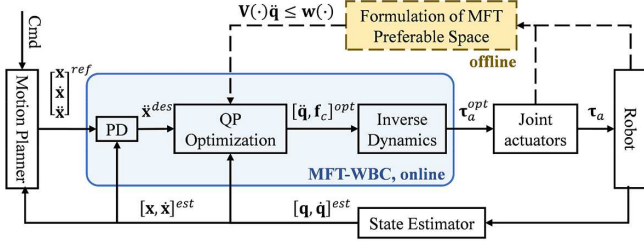


Fig. 2. The locomotion control architecture. The solid lines and boxes denote the online parts, and the dashed ones denote the offline parts.

We first establish the MFT preferable space of the robot and formulate it as a polyhedron in the joint space at the acceleration level. Then, the WBC employs the polyhedron as a soft constraint. As a result, the robot possesses high-speed and high-acceleration capabilities by maintaining the joints within the MFT preferable space. We test our scheme on a parallel-legged bipedal robot in Fig. 1. The weight of the robot is 23.5kg. We deliberately install 4 heavy calves on the robot, so that the mass ratio between the legs and the torso is about 40%, which is not negligible according to [23]. The results show that, with the proposed WBC scheme, the robot can achieve robust locomotion with external disturbances.

The rest of the paper is organized as follows. Sec. II introduces the definition of MFT preferable space and discusses the MFT formulation. Sec. III states our proposed MFT-WBC scheme. Sec. IV demonstrates the advantage of MFT-WBC in improving the robustness of the system through the tests on the parallel-legged bipedal robot. Finally, Sec. V concludes this paper.

## II. MFT PREFERABLE SPACE

Our locomotion control architecture is shown in Fig. 2. First, a state estimator provides the current robot states  $\mathbf{x}^{est}$ . Given the user command, a motion planner generates the reference trajectories  $\mathbf{x}^{ref}$  according to the robot states. Then the MFT-WBC generates optimized joint torques  $\boldsymbol{\tau}_a^{opt}$  to track these trajectories and comply with specific physical constraints. We focus on the offline MFT formulation and the online WBC scheme. In this section, we first introduce the evaluation of MFT briefly, then discuss the MFT formulation in the context of our control scheme.

### A. Evaluation of MFT

MFT is an essential feature having a significant influence on the kinematic and dynamic performance of parallel robots in many aspects [19]. LTI is a commonly used index to represent the local MFT of the parallel robot with a given configuration [20], and is expressed as:

$$\gamma_{LTI} = \min \{ \gamma_I, \gamma_O \} \quad (1a)$$

$$\gamma_I = \min \left\{ \frac{|\$T_1 \circ \$I_1|}{|\$T_1 \circ \$I_1|_{\max}}, \dots, \frac{|\$T_{n_l} \circ \$I_{n_l}|}{|\$T_{n_l} \circ \$I_{n_l}|_{\max}} \right\} \quad (1b)$$

$$\gamma_O = \min \left\{ \frac{|\$T_1 \circ \$O_1|}{|\$T_1 \circ \$O_1|_{\max}}, \dots, \frac{|\$T_{n_l} \circ \$O_{n_l}|}{|\$T_{n_l} \circ \$O_{n_l}|_{\max}} \right\} \quad (1c)$$

where  $n_l$  is the number of the limbs,  $\$T$ ,  $\$I$  and  $\$O$  denote the transmission wrench, input twist and output twist of the limb, respectively. By calculating the minimal ratio of the instantaneous input power  $|\$T \circ \$I|$  and its potential maximum value  $|\$T \circ \$I|_{\max}$ ,  $\gamma_I$  is used to evaluate the input MFT. Similarly,  $\gamma_O$  is used to evaluate the output MFT. the index  $\gamma_{LTI} \in [0, 1]$  is dimensionless. Larger  $\gamma_{LTI}$  means better MFT. When  $\gamma_{LTI}$  tends to 0, the robot tends to the input or output singularity. In addition, we also consider the RACI, which represents the acceleration capacity of the parallel robot with a given configuration and is expressed as:

$$\gamma_{RACI} = \max \{ \tau_{N1}, \dots, \tau_{Nn_l} \}, \quad (2)$$

where  $\tau_N$  is the normalized joint torque in the worst case with the predefined maximum translational and rotational accelerations  $[\ddot{\mathbf{x}}_t, \ddot{\mathbf{x}}_r]$ . The term  $\tau_N$  is a nonlinear function of  $|\$T \circ \$I|$ ,  $|\$T \circ \$O|$ , the inertial parameters of the robot, and the specifications of the actuators. Refer to [24] for its detailed derivation. A configuration with greater  $\gamma_{RACI}$  indicates the robot requires larger joint torques to achieve the predefined acceleration.

An intuitive approach to bring MFT in a control scheme is to restrict the robot within a workspace in which it possesses promising MFT, resulting in the following definition.

**Definition 1 (MFT preferable space):** Let  $\gamma$  denotes a set of MFT indices, and  $[\underline{\gamma}, \overline{\gamma}]$  denotes an user-defined reasonable range of each index. A workspace  $\gamma\mathbf{Q}$  of a parallel mechanism is the MFT preferable space with respect to  $\gamma$ , if and only if,  $\forall \mathbf{p} \in \gamma\mathbf{Q}, \forall \gamma \in \gamma: \underline{\gamma} \leq \gamma(\mathbf{p}, \Phi) \leq \overline{\gamma}$ , where  $\Phi$  denotes the parameters of the parallel mechanism.

### B. Formulation of MFT Preferable Space

Generally, the MFT preferable space has nonlinear relationship with the robot's configuration. To formulate the MFT preferable space as a constraint in the QP-based WBC, we first approximate the robot's MFT preferable space as a polyhedron, then convert the resulting polyhedron into a polyhedron in the generalized joint space at the acceleration level.

For each parallel mechanism in a parallel-legged robot, we first discretize the reachable space of its end effector in the Cartesian space with user-defined resolution. Then, we get the gridded MFT preferable space  $\gamma\mathbf{Q}_g$  by traversing both the former discretized reachable space and the given indices set  $\gamma$ , according to Definition 1. Hereafter, we approximate  $\gamma\mathbf{Q}_g$  with a 3-dimensional polyhedron  $\mathbf{P}^3$  conservatively using the method provided by [25]. The polyhedron  $\mathbf{P}^3$  can be expressed as the intersection of several halfspaces in the form of  $\mathbf{A}\mathbf{p} \leq \mathbf{b}$ . This approximation must fulfill the following conditions:

- 1)  $\forall \mathbf{p} \in \mathbf{P}_g^3: \mathbf{p} \in \gamma\mathbf{Q}_g$ ,
- 2)  $\forall \mathbf{p} \notin \mathbf{P}_g^3 \wedge \mathbf{p} \in \gamma\mathbf{Q}_g: d_{\min}^{\mathbf{p} \rightarrow \text{bd}\{\mathbf{P}^3\}} \leq \underline{d}$ ,

where  $\mathbf{P}^3$  is the gridded  $\mathbf{P}^3$  with the same resolution as  $\gamma\mathbf{Q}_g$ ,  $d_{\min}^{\mathbf{p} \rightarrow \text{bd}\{\mathbf{P}^3\}}$  denotes the shortest distance from the point  $\mathbf{p}$  to the boundary of  $\mathbf{P}^3$ , and  $\underline{d} \geq 0$  is a scalar reflecting the conservative degree of the approximation.

By exploring all the parallel mechanisms and stacking  $\mathbf{A}$ ,  $\mathbf{b}$ , we can obtain the resulting polyhedron of MFT preferable space in the workspace for the robot:

$$\mathbf{P}_p^m = \{\mathbf{p} \in \mathbb{R}^m | \mathbf{A}\mathbf{p} \leq \mathbf{b}\}, \quad (3)$$

where  $\mathbf{A} \in \mathbb{R}^{n_h \times m}$ ,  $\mathbf{b} \in \mathbb{R}^{n_h}$ ,  $n_h$  is the number of halfspaces in the polyhedron,  $m = 3n_s$  denotes the dimension of the polyhedron, and  $n_s$  is the number of parallel mechanisms.

Since the generalized acceleration vector  $\ddot{\mathbf{q}}$  is one of the optimization variables, the polyhedron  $\mathbf{P}_p^m$  should be converted to a polyhedron in the generalized joint space at the acceleration level:

$$\mathbf{P}_{\ddot{\mathbf{q}}}^n = \{\ddot{\mathbf{q}} \in \mathbb{R}^n | \mathbf{V}\ddot{\mathbf{q}} \leq \mathbf{w}\}, \quad (4)$$

where  $\mathbf{V} \in \mathbb{R}^{n_h \times n}$ ,  $\mathbf{w} \in \mathbb{R}^{n_h}$ ,  $n$  is the dimension of the generalized joint space. This conversion can be conducted by approximating  $\mathbf{p}$  with its Taylor expansion around the current instant  $\hat{t}$ . For the  $k^{\text{th}}$  element of  $\mathbf{p}$ , the position after an interval  $\Delta t$  from  $\hat{t}$  can be approximated as  $\tilde{p}_k$ :

$$\begin{aligned} \tilde{p}_k &\cong \hat{p}_k + \hat{\dot{p}}_k + \frac{1}{2} \hat{\ddot{p}}_k \Delta t^2 \\ &= \hat{p}_k + \mathbf{J}_{(k,:)} \hat{\dot{\mathbf{q}}} \Delta t + \frac{1}{2} \left( \mathbf{J}_{(k,:)} \hat{\ddot{\mathbf{q}}} + [\dot{\mathbf{J}}\dot{\mathbf{q}}]_k \right) \Delta t^2, \end{aligned} \quad (5)$$

where the terms with hat represent the values at  $\hat{t}$ , the subscript  $(k, :)$  denotes the  $k^{\text{th}}$  row in a matrix. The terms  $\mathbf{J}$  and  $\dot{\mathbf{J}}\dot{\mathbf{q}}$  satisfy  $\dot{\mathbf{p}} = \mathbf{J}\dot{\mathbf{q}}$  and  $\ddot{\mathbf{p}} = \mathbf{J}\ddot{\mathbf{q}} + \dot{\mathbf{J}}\dot{\mathbf{q}}$ , where  $\mathbf{J}$  is the Jacobian of the end effector. Substituting (5) into (3), the polyhedron defined in (4) can be then obtained as:

$$\mathbf{V}_{(i,j)} = \frac{1}{2} \Delta t^2 \sum_{k=1}^m (\mathbf{A}_{(i,k)} \mathbf{J}_{(k,j)}), \quad (6)$$

and

$$\mathbf{w}_i = \mathbf{b}_i - \sum_{k=1}^m \left( \mathbf{A}_{(i,k)} \left( \hat{\mathbf{p}}_k + \mathbf{J}_{(k,:)} \hat{\dot{\mathbf{q}}} \Delta t + \frac{1}{2} [\dot{\mathbf{J}}\dot{\mathbf{q}}]_k \Delta t^2 \right) \right), \quad (7)$$

where the subscript  $(i, j)$  denotes the entry of a matrix.

As shown in Fig. 2, the offline formulation of MFT preferable space outputs the structure of  $\mathbf{V}(\cdot)$  and  $\mathbf{w}(\cdot)$ . The WBC will employ  $\mathbf{P}_{\ddot{\mathbf{q}}}^n$  as a constraint to enhance the MFT performance during locomotion.

### III. WHOLE-BODY CONTROL SCHEME

In this section, we formulate the MFT-WBC as a QP in Formulation 1. All the tasks and constraints are written as affine functions of the optimization variables, which will be explained in detail in the following subsections.

#### A. Dynamic Consistency of the Parallel-Legged Robot

A parallel-legged robot can be modeled as a rigid-body system with holonomic constraints caused by closed-loop chains, and the system dynamics can be written as:

$$\begin{bmatrix} \mathbf{M} & -\mathbf{J}_h^T \\ \mathbf{J}_h & \mathbf{0} \end{bmatrix} \begin{bmatrix} \ddot{\mathbf{q}} \\ \mathbf{f}_h \end{bmatrix} = \begin{bmatrix} \mathbf{S}_a^T \boldsymbol{\tau}_a + \mathbf{J}_c^T \mathbf{f}_c - \mathbf{H} \\ -\dot{\mathbf{J}}_h \dot{\mathbf{q}} \end{bmatrix}, \quad (17)$$

where  $\mathbf{q} \in \mathbb{R}^n$  denotes the generalized coordinates, including the position and orientation of the floating base, as well as the position of the actuated and underactuated joints. the term

Formulation 1 QP of MFT-WBC for Parallel-Legged Robot Locomotion	
Trajectory tracking	$\min_{\ddot{\mathbf{q}}, \mathbf{f}_c, \epsilon} \left\  \mathbf{J}_x \ddot{\mathbf{q}} + \dot{\mathbf{J}}_x \dot{\mathbf{q}} - \ddot{\mathbf{x}}^{des} \right\ _{\mathbf{w}_x}^2 +$ (8)
Closed-loop chains	$\left\  \mathbf{J}_h \ddot{\mathbf{q}} + \dot{\mathbf{J}}_h \dot{\mathbf{q}} \right\ _{\mathbf{w}_h}^2 +$ (9)
Penalty on forces	$\left\  \mathbf{f}_c \right\ _{\mathbf{w}_{f_c}}^2 + \left\  \mathbf{f}_c - \mathbf{f}_c^- \right\ _{\mathbf{w}_{\delta f_c}}^2 +$ (10)
Relaxation on MFT	$\left\  \epsilon \right\ _{\mathbf{w}_\epsilon}^2$ (11)
Dynamic consistency	s.t. $\mathbf{S}_f (\mathbf{M} \ddot{\mathbf{q}} + \mathbf{N}_h^T \mathbf{H}) = \mathbf{S}_f \mathbf{N}_h^T \mathbf{J}_c^T \mathbf{f}_c$ (12)
Forces constraints	$\mathbf{U} \mathbf{f}_c \leq \mathbf{u}$ (13)
MFT preferable space	$\mathbf{V} \ddot{\mathbf{q}} \leq \mathbf{w} + \epsilon$ (14)
Joint limits	$\mathbf{q}_s^{\min} \leq \mathbf{S}_s \mathbf{q} \leq \mathbf{q}_s^{\max}$ (15)
Torque limits	$\boldsymbol{\tau}_a^{\min} \leq \boldsymbol{\tau}_a(\ddot{\mathbf{q}}, \mathbf{f}_c) \leq \boldsymbol{\tau}_a^{\max}$ (16)

$\mathbf{M}$  is the inertia matrix,  $\mathbf{H}$  is the vector that accounts for Coriolis, centrifugal and gravitational forces. The vector  $\boldsymbol{\tau}_a$  is the torque vector of actuated joints, and the matrix  $\mathbf{S}_a$  is the actuation matrix selecting actuated degrees of freedom. The vector of contact forces  $\mathbf{f}_c$  is mapped to the generalized joint space through the combined contact Jacobian  $\mathbf{J}_c$ . A similar relationship can be found between the internal closed-loop holonomic constraint forces  $\mathbf{f}_h$  and its corresponding Jacobian  $\mathbf{J}_h$ .

By eliminating  $\mathbf{f}_h$ , an equation that fully describes the dynamics of the internal constrained system can be obtained as:

$$\mathbf{M} \ddot{\mathbf{q}} + \mathbf{N}_h^T \mathbf{H} + \mathbf{J}_h^T \boldsymbol{\Lambda}_h \dot{\mathbf{J}}_h \dot{\mathbf{q}} - \mathbf{N}_h^T \mathbf{S}_a^T \boldsymbol{\tau}_a = \mathbf{N}_h^T \mathbf{J}_c^T \mathbf{f}_c, \quad (18)$$

where,  $\boldsymbol{\Lambda}_h = (\mathbf{J}_h \mathbf{M}^{-1} \mathbf{J}_h^T)^{-1}$ ,  $\mathbf{J}_h^\# = \mathbf{M}^{-1} \mathbf{J}_h^T \boldsymbol{\Lambda}_h$ , and  $\mathbf{N}_h = \mathbf{I} - \mathbf{J}_h^\# \mathbf{J}_h$  denote the apparent inertia, dynamically consistent inverse, and null space projector of the holonomic constraint, respectively. The floating-base dynamics (12) can be derived from (18) with the floating-base selection matrix  $\mathbf{S}_f$ , and the last two terms in the left-hand-side of (18) is canceled, since the internal forces have no influence on the centroidal dynamics [26]. Notably, the equality constraint  $\mathbf{J}_h \ddot{\mathbf{q}} = -\dot{\mathbf{J}}_h \dot{\mathbf{q}}$  is not stable during numerical integration [14]. Consequently, we relax this equality in the cost as (9) in Formulation 1.

#### B. Legged Locomotion Tasks

Trajectory tracking task can be phrased as  $\ddot{\mathbf{x}}^{des} = \mathbf{J}_x \ddot{\mathbf{q}} + \dot{\mathbf{J}}_x \dot{\mathbf{q}}$ , where  $\mathbf{J}_x$  is the task Jacobian and  $\ddot{\mathbf{x}}^{des}$  is the desired task acceleration that corresponds to a PD control as shown in Fig. 2. We try to minimize the weighted Euclidean distance of the tracking error in the QP, resulting in (8).

To avoid slipping and flipping, we constrain the contact forces to keep them inside the friction cone and bound the contact torques of each contact link as:

$$|f_t| \leq \mu f_n, \quad 0 \leq f_n \leq \bar{f}, \quad (19a)$$

$$|f_{m,x}| \leq \frac{d_y}{2} f_n, \quad |f_{m,y}| \leq \frac{d_x}{2} f_n, \quad (19b)$$

where  $f_n$ ,  $f_t$  and  $f_m$  denote the normal force, tangential force, and reaction torque on a local terrain frame, respectively. The term  $\bar{f}$  denotes the upper bound of  $f_n$ ,  $d_x$  and  $d_y$  are the lengths and widths of the contact surface. By

performing frame rotations and approximating the friction cones with pyramids [9], we can get the augmented linear constraint (13) for all the feet compactly.

To avoid jumps in the actuation signals when a leg is switching between support and swing phase, the QP takes two measures. First, we penalize changes in contact forces by the second term of (10). Second, we modulate  $f_n$  according to the motion plan by gradually decreasing  $\tilde{f}$  to zero before lift-off, and increasing  $\tilde{f}$  from zero on touch-down [27]. Working as a regularization to  $\mathbf{f}_c$ , the first term of (10) aims to improve energetic efficiency.

The joint and torque limits are enforced in the inequality constraints (15) and (16), respectively, where  $\mathbf{S}_s$  selects the concerned joints. To have linear inequality about  $\dot{\mathbf{q}}$  and  $\mathbf{f}_c$ , we approximate  $\mathbf{q}$  with its Taylor expansion around the current instant. Additionally, we obtain the coefficient matrix and boundary vector for  $\boldsymbol{\tau}_a$  using:

$$\mathbf{S}_a(\mathbf{M}\ddot{\mathbf{q}} + \mathbf{N}_h^T \mathbf{H} + \mathbf{J}_h^T \mathbf{A}_h \dot{\mathbf{J}}_h \dot{\mathbf{q}}) = \mathbf{S}_a(\mathbf{N}_h^T \mathbf{S}_a^T \boldsymbol{\tau}_a + \mathbf{N}_h^T \mathbf{J}_c^T \mathbf{f}_c). \quad (20)$$

### C. MFT as the Soft Constraint

In our WBC scheme, to enhance the MFT performance, the polyhedron of MFT preferable space is employed in (14) of Formulation 1. We introduce the relax variable  $\epsilon$  for the MFT preferable space so it can be easily implemented as a soft constraint to the QP-based WBC method. Furthermore, we can tune its corresponding weight with respect to the executing tasks conveniently. The relax variable  $\epsilon$  is minimized by (11) during optimization. The values of  $\mathbf{V}$  and  $\mathbf{w}$  are updated online with (6) and (7) according to the current states  $\hat{\mathbf{p}}$ ,  $\hat{\mathbf{q}}$ ,  $\dot{\hat{\mathbf{q}}}$  and the time interval  $\Delta t$ .

At this point the proposed MFT-WBC is fully specified. Formulation 1 uses weights  $\mathbf{W}_*$  to embody the relative priority among tasks \*. Solving the QP and (20) yields the control command  $\boldsymbol{\tau}_a^{opt}$ .

## IV. SIMULATIONS AND EXPERIMENTS

In this section we discuss the implementation in detail and show the results obtained from the simulations and experiments with the MFT-WBC scheme.

### A. Implementation Details

As shown in Fig. 1, with the torso constrained by a boom, the bipedal robot can move and pitch within the sagittal plane. Each leg of the robot is composed of a five-bar linkage mechanism, which is actuated by two identical series elastic actuators (SEAs) at fore and rear hip joints. We model the robot as a rigid body system consists of 11 generalized coordinates  $\mathbf{q} = [q_1, q_2, \dots, q_{11}]^T$  (3 for the floating-base  $B$  with respect to the inertial frame  $I$ , 4 for actuated hip joints, 4 for underactuated knee joints), 2 closed-loop holonomic constraints at passive ankles, and 4 contact forces of feet  $\mathbf{f}_c = [f_1^x, f_1^z, f_2^x, f_2^z]^T$ .

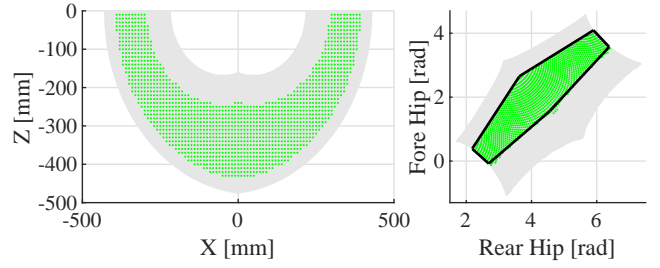


Fig. 3. The MFT preferable space for each leg in the Cartesian space (left) and the actuated joint space (right). The light gray area denotes its reachable space, and the gridded green area denotes its gridded MFT preferable space.

1) *Motion Planner Setup*: The user-defined height of  $B$  and an average sagittal speed (i.e.,  $[Iz_B^{cmd}, \bar{v}^{cmd}]^T$ ) are the inputs of the motion planner. The planner outputs the trajectories of the floating-base and feet with respect to the frame  $I$  according to robot states. Due to the underactuated nature of the bipedal walking, only the height and pitch of the floating-base are planned, leaving its sagittal movement as a passive dynamic process:

$$Iz_B^{ref} = Iz_B^{cmd}, \quad I\theta_B^{ref} = 0, \quad (21)$$

The trajectory of the support foot is required to maintain its current location. The swing foot planning aims to regulate the average sagittal speed of the floating-base towards  $\bar{v}^{cmd}$ . We plan the target pre-impact foot placement with a PD control [28], [29]:

$$I\dot{x}_{sw}^* = I\dot{x}_C + k_v I\dot{x}_C + k_p (I\dot{x}_C - I\dot{x}_C^*) \quad (22)$$

where  $[I\dot{x}_C, I\dot{x}_C^*]^T$  is the predicted horizontal pre-impact center of mass (CoM) state [30],  $I\dot{x}_C^*$  is the desired pre-impact CoM speed determined by  $\bar{v}^{cmd}$  [31]. We set  $k_v = 0.16$ ,  $k_p = 0.08$  in this application. The nominal step duration of the walking gait is 0.35 sec.

2) *MFT-WBC Setup*: The indices LTI and RACI are used to evaluate the MFT. We set  $\gamma_{LTI} \geq 0.7$  based on prior knowledge, and set  $\gamma_{RACI} \leq 174.54 \text{ N}/\sqrt{\text{kg}}$  based on the specifications of the actuators, so that a maximum acceleration  $60 \text{ m/s}^2$  at the foot can be achieved during locomotion. We obtain the gridded MFT preferable space  $\gamma\mathbf{Q}_g$  in the workspace for each leg with a resolution  $10 \times 10 \text{ mm}$ , as shown in the left-hand-side of Fig. 3. However, for the planar robot in Fig. 1, it is more convenient to conduct polyhedron approximation in its actuated joint space, as shown in the right-hand-side of Fig. 3. In the actuated joint space, the gridded MFT preferable space  $\gamma\mathbf{Q}_g^a$  corresponding to  $\gamma\mathbf{Q}_g$  individually with inverse kinematics can be approximated by a hexagon, whose boundaries are marked by black solid lines. The robot's polyhedron of MFT preferable space in the actuated joint space can be expressed as  $\mathbf{P}_a^4 = \{\mathbf{q}_a \in \mathbb{R}^4 | \mathbf{A}\mathbf{q}_a \leq \mathbf{b}\}$ , where  $\mathbf{q}_a = [q_4, q_6, q_8, q_{10}]^T$ . Then the polyhedron  $\mathbf{P}_{\ddot{\mathbf{q}}}^{11} = \{\ddot{\mathbf{q}} \in \mathbb{R}^{11} | \mathbf{V}\ddot{\mathbf{q}} \leq \mathbf{w}\}$  can be obtained with (6) and (7) by replacing  $\hat{\mathbf{p}}$  and  $\mathbf{J}$  with  $\hat{\mathbf{q}}_a$  and  $\mathbf{S}_a$ , respectively.

We construct the WBC as Formulation 1 with optimization variables  $[\ddot{\mathbf{q}}^T, \mathbf{f}_c^T, \epsilon^T]^T \in \mathbb{R}^{27}$ , where  $\epsilon \in \mathbb{R}^{12}$  corresponds



TABLE I  
WEIGHTS OF TASKS

$w_z$	$w_\theta$	$w_{foot}^{sw}$	$w_{foot}^{st}$	$w_h$	$w_{fc}$	$w_{\delta fc}$	$w_\epsilon$
1	1	1	1e2	1e5	1e-3	5e-2	1e3

TABLE II  
RESULTS OF PUSH-RECOVERY TESTS IN SIMULATION

$I_{z_B}^{ref}$ [m]	0.38	0.40	0.42	0.44	0.46
$I_{max}$ of noMFT-WBC [Ns]	10.4	9.7	9.1	7.0	4.5
$I_{max}$ of MFT-WBC [Ns]	10.7	10.6	10.6	9.5	6.6
Percentage of Increase [%]	2.9	9.3	16.5	35.6	44.4

to 12 hyperspaces (6 boundaries of MFT preferable space for each leg). The WBC utilizes RBDL [32] for rigid body dynamics and qpOASES [33] as the QP solver, running at 1 kHz. Since the SEA shows an average settling time of  $\bar{t}_s = 0.025$  sec for step torque signals, we set  $\Delta t = 2\bar{t}_s$  for the prediction (5) empirically. The weights of tasks are specified in Table I, where  $w_z$ ,  $w_\theta$ ,  $w_{foot}^{sw}$ , and  $w_{foot}^{st}$  denote the weights for tracking trajectories of floating-base, swing foot and support foot, respectively. And the terms  $w_h$ ,  $w_{fc}$ ,  $w_{\delta fc}$  and  $w_\epsilon$  are the diagonal elements of  $\mathbf{W}_h$ ,  $\mathbf{W}_{fc}$ ,  $\mathbf{W}_{\delta fc}$  and  $\mathbf{W}_\epsilon$ , respectively.

### B. Simulations for Comparative Verification

To verify the proposed method, we conducted several push-recovery tests for the bipedal robot in simulation. The simulation environment is the open-source robot simulator Webots. Two different schemes were tested: One was the proposed MFT-WBC with the setup in Sec. IV-A.2; The other one, labeled noMFT-WBC, was exactly the same as the former one, except that it removed the MFT terms formulated in (11), (14). For every test, while stepping in place, the robot received a sagittal impulse at the moment when its left foot just lifted off. The impulse magnitude started at 3 Ns and increased in a step of 0.1 Ns until we found the maximum impulse  $I_{max}$ , from which the robot could recover.

Five groups of the above tests were conducted with different reference height of floating-base  $I_{z_B}^{ref}$ , and the results are shown in Table II. For the first three groups of tests, the heights  $I_{z_B}^{ref}$  were less than 0.43 m, which were relatively good plannings. This is because when maintaining these floating-base heights (0.38 m, 0.40 m, 0.42 m) to step in place, the robot's legs were naturally within their MFT preferable space. On the contrary, the last two groups of tests were with relatively bad plannings, since the robot's support legs were always outside their MFT preferable space when stepping in place.

The results in Table II show that, compared with noMFT-WBC, the MFT-WBC can improve the robustness of the system. The maximum sustainable impulse increased 16.5% for the relatively good plannings, and 44.4% for the relatively bad plannings. With a worse planning, the proposed scheme can correct the trajectory to satisfy the MFT preferable space.

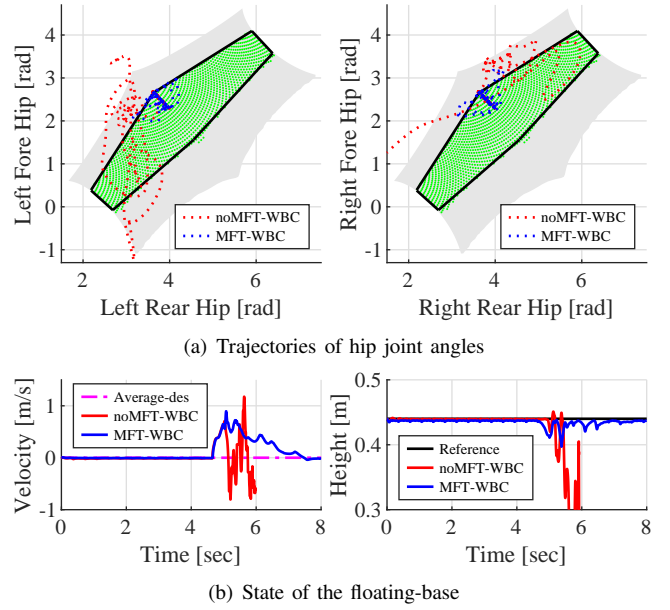


Fig. 4. Simulation results for the case  $I_{z_B}^{ref} = 0.44\text{m}$ ,  $I = 7.1\text{Ns}$

Consequently, the performance as percentage is increased significantly comparing with noMFT-WBC.

For the case  $I_{z_B}^{ref} = 0.44$  m, by applying  $I = 7.1$  Ns, the result trajectories of the hip joint angles are shown in Fig. 4 (a), and the state of the floating-base is shown in Fig. 4 (b). For the robot with MFT-WBC, when stepping without external impulse, the actual height of the floating-base was about 0.43 m and the legs stayed within the MFT preferable space. After receiving the impulse at 4.66 sec, the MFT-WBC tried to keep the robot in the specified MFT preferable space by sacrificing the execution of other tasks, such as the height of the floating-base, resulting in that the robot retained a desired MFT and kept away from its singularity. Finally, the robot recovered from the external disturbance. However, under the same external impulse, the scheme noMFT-WBC diverged and the robot reached its singularity, although singular avoidance constraint was considered through (15). If the leg is outside the MFT preferable space but within the reachable boundary, sustaining the same impulse requires significant joint torques that the actuators can not exert, due to the MFT is poor. These results demonstrate the advantage of MFT-WBC in improving the robustness of the system, and similar results can be obtained from other groups of tests with different plannings and impulse magnitudes.

### C. Experimental Results

As shown in Fig. 5, we conducted two experiments on the robot in Fig. 1 with the proposed MFT-WBC.

1) *Push Recovery*: Similar to the simulation, during stepping in place, the robot was hit by a 5 kg (21% of robot's weight) wall ball in the sagittal direction for 12 times. The sagittal velocity of the floating-base is shown in Fig. 6 (a), the robot recovered from instant velocity change up to 0.9 m/s. The state of the floating-base around the second push is

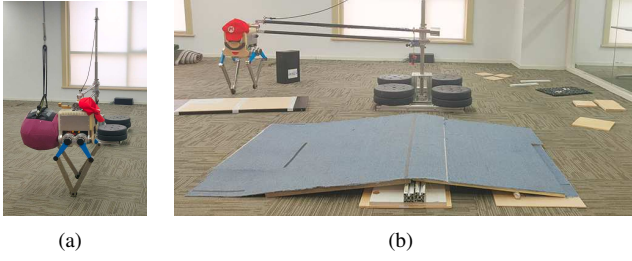


Fig. 5. (a) Push recovery. (b) Uneven terrain. In (b), the robot blindly walked through a 3 cm board, a 6° slope, as well as some rough terrains about 2 cm high composed of wooden/rubber boards and pebbles, tracking the specified average speed and upper body posture.

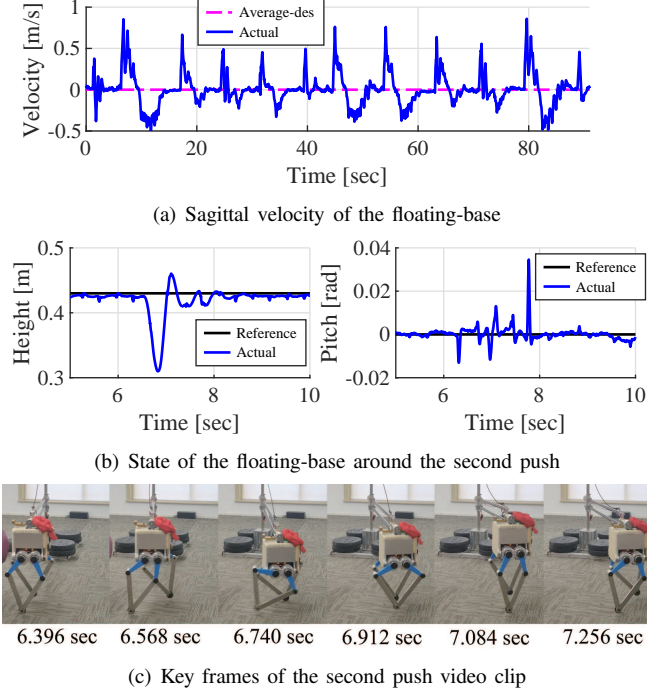


Fig. 6. Push recovery results

presented in Fig. 6 (b), and the key frames within 1 sec after the second push is shown in Fig. 6 (c). As we can see, the right leg was about to reach its singularity after 6.568 sec. In this situation, the MFT constraint lowered the height of the robot to keep the legs within their MFT preferable space. The MFT-WBC enhanced the robustness of the system by considering the MFT preferable space, which was essential to the recovery of the robot. Consequently, the execution of the latter tasks was ensured.

2) *Uneven Terrain*: The robot successfully passed the uneven terrain test in Fig. 5 (b). The experimental data collected during uneven terrain locomotion are shown in Fig. 7. In Fig. 7 (b), the MFT preferable space was well satisfied with jump-free torques. And the robot could track the reference state of the floating-base with acceptable errors. These results demonstrate the functionalities of MFT-WBC, including trajectory tracking, slippage prevention, jump avoidance of torque command and MFT consideration feature.

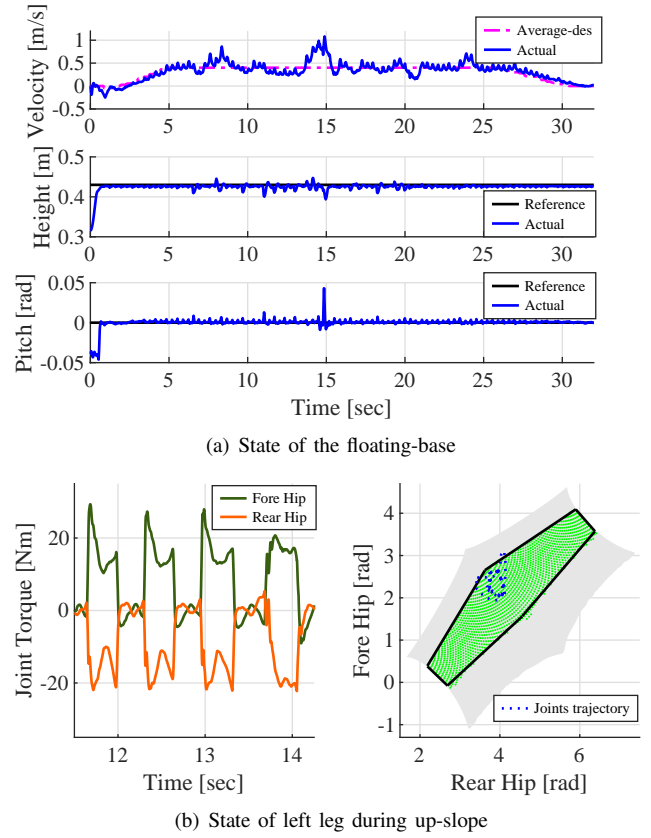


Fig. 7. Uneven terrain results

In both experiments, the planner and controller had no prior information of push or terrain. By considering the proposed MFT preferable space as the constraint, the MFT-WBC improves the robustness and perceptionless adaptability of the robot under external disturbances.

## V. CONCLUSIONS

This paper proposed the MFT-WBC scheme for robust locomotion of parallel-legged robots. The MFT preferable space is considered as a soft constraint in the QP-based WBC to enhance the robot's MFT performance. Through the comparative simulations, we verified the advantage of MFT-WBC, which improved the robustness of the system. The experimental results showed that, with the proposed MFT-WBC scheme, the parallel-legged robot achieved blindly walking over uneven terrain and push recovery without trajectory re-planning. Besides, the polyhedral approximation method for MFT formulation proposed in this paper is also applicable to the other dynamic performance indices in WBC, such as manipulability ellipsoid. Our future work includes two aspects: 1) extend the preferable space discretization method to other dynamic performance for robots; 2) consider MFT in the locomotion planning methods.

## REFERENCES

- [1] C. Hubicki, J. Grimes, M. Jones, D. Renjewski, A. Spröwitz, A. Abate, and J. Hurst, "Atrias: Design and validation of a tether-free 3D-capable spring-mass bipedal robot," *The International Journal of Robotics Research*, vol. 35, no. 12, pp. 1497–1521, 2016.

- [2] X. Xiong and A. D. Ames, "Bipedal hopping: Reduced-order model embedding via optimization-based control," in *2018 IEEE/RSJ International Conference on Intelligent Robots and Systems (IROS)*. IEEE, 2018, pp. 3821–3828.
- [3] G. A. Castillo, B. Weng, W. Zhang, and A. Hereid, "Robust feedback motion policy design using reinforcement learning on a 3D digit bipedal robot," *arXiv preprint arXiv:2103.15309*, 2021.
- [4] D. Neil and S.-C. Liu, "Minitaur, an event-driven fpga-based spiking network accelerator," *IEEE Transactions on Very Large Scale Integration (VLSI) Systems*, vol. 22, no. 12, pp. 2621–2628, 2014.
- [5] S. Wang, L. Cui, J. Zhang, J. Lai, Z. Dongsheng, K. Chen, Y. Zheng, Z. Zhang, and Z.-P. Jiang, "Balance control of a novel wheel-legged robot: design and experiments," in *2021 IEEE International Conference on Robotics and Automation (ICRA 2021)*. IEEE, 2021, pp. 6782–6788.
- [6] E. Yoshida, O. Kanoun, C. Esteves, and J.-P. Laumond, "Task-driven support polygon reshaping for humanoid," in *2006 6th IEEE-RAS International Conference on Humanoid Robots*. IEEE, 2006, pp. 208–213.
- [7] L. Sentis and O. Khatib, "A whole-body control framework for humanoid operating in human environments," in *Proceedings 2006 IEEE International Conference on Robotics and Automation, 2006. ICRA 2006*. IEEE, 2006, pp. 2641–2648.
- [8] O. Kanoun, J.-P. Laumond, and E. Yoshida, "Planning foot placements for a humanoid robot: A problem of inverse kinematics," *The International Journal of Robotics Research*, vol. 30, no. 4, pp. 476–485, 2011.
- [9] J. W. Grizzle, C. Chevallereau, R. W. Sinnet, and A. D. Ames, "Models, feedback control, and open problems of 3d bipedal robotic walking," *Automatica*, vol. 50, no. 8, pp. 1955–1988, 2014.
- [10] H. Dai, A. Valenzuela, and R. Tedrake, "Whole-body motion planning with centroidal dynamics and full kinematics," in *2014 IEEE-RAS International Conference on Humanoid Robots*. IEEE, 2014, pp. 295–302.
- [11] M. Hutter, H. Sommer, C. Gehring, M. Hoepflinger, M. Bloesch, and R. Siegwart, "Quadrupedal locomotion using hierarchical operational space control," *The International Journal of Robotics Research*, vol. 33, no. 8, pp. 1047–1062, 2014.
- [12] S. Feng, E. Whitman, X. Xinjilefu, and C. G. Atkeson, "Optimization-based full body control for the darpa robotics challenge," *Journal of Field Robotics*, vol. 32, no. 2, pp. 293–312, 2015.
- [13] A. Herzog, N. Rotella, S. Mason, F. Grimmering, S. Schaal, and L. Righetti, "Momentum control with hierarchical inverse dynamics on a torque-controlled humanoid," *Autonomous Robots*, vol. 40, no. 3, pp. 473–491, 2016.
- [14] R. Featherstone, *Rigid body dynamics algorithms*. Springer, 2014.
- [15] T. Apgar, P. Clary, K. Green, A. Fern, and J. W. Hurst, "Fast online trajectory optimization for the bipedal robot Cassie," in *Robotics: Science and Systems*, vol. 101, 2018, p. 14.
- [16] D. Kim, J. Lee, J. Ahn, O. Campbell, H. Hwang, and L. Sentis, "Computationally-robust and efficient prioritized whole-body controller with contact constraints," in *2018 IEEE/RSJ International Conference on Intelligent Robots and Systems (IROS)*. IEEE, 2018, pp. 1–8.
- [17] J. Reher, C. Kann, and A. D. Ames, "An inverse dynamics approach to control lyapunov functions," in *2020 American Control Conference (ACC)*. IEEE, 2020, pp. 2444–2451.
- [18] C. Chen and J. Angeles, "Generalized transmission index and transmission quality for spatial linkages," *Mechanism and Machine Theory*, vol. 42, no. 9, pp. 1225–1237, 2007.
- [19] J. Wang, C. Wu, and X.-J. Liu, "Performance evaluation of parallel manipulators: Motion/force transmissibility and its index," *Mechanism and Machine Theory*, vol. 45, no. 10, pp. 1462–1476, 2010.
- [20] X.-J. Liu, C. Wu, and J. Wang, "A new approach for singularity analysis and closeness measurement to singularities of parallel manipulators," *Journal of Mechanisms and Robotics*, vol. 4, no. 4, 2012.
- [21] X.-J. Liu, G. Han, F. Xie, and Q. Meng, "A novel acceleration capacity index based on motion/force transmissibility for high-speed parallel robots," *Mechanism and Machine Theory*, vol. 126, pp. 155–170, 2018.
- [22] J. Brinker, B. Corves, and Y. Takeda, "Kinematic performance evaluation of high-speed delta parallel robots based on motion/force transmission indices," *Mechanism and Machine Theory*, vol. 125, pp. 111–125, 2018.
- [23] D. Kim, S. J. Jorgensen, H. Hwang, and L. Sentis, "Control scheme and uncertainty considerations for dynamic balancing of passive-ankled bipeds and full humanoids," in *2018 IEEE-RAS 18th International Conference on Humanoid Robots (Humanoids)*. IEEE, 2018, pp. 1–9.
- [24] G. Han, F. Xie, X.-J. Liu, Q. Meng, and S. Zhang, "Technology-oriented synchronous optimal design of a 4-degrees-of-freedom high-speed parallel robot," *Journal of Mechanical Design*, vol. 142, no. 10, 2020.
- [25] D. S. Lo, *Finite element mesh generation*. CRC Press, 2014.
- [26] P. M. Wensing and D. E. Orin, "Improved computation of the humanoid centroidal dynamics and application for whole-body control," *International Journal of Humanoid Robotics*, vol. 13, no. 01, p. 1550039, 2016.
- [27] C. D. Bellicoso, C. Gehring, J. Hwangbo, P. Fankhauser, and M. Hutter, "Perception-less terrain adaptation through whole body control and hierarchical optimization," in *2016 IEEE-RAS 16th International Conference on Humanoid Robots (Humanoids)*. IEEE, 2016, pp. 558–564.
- [28] M. H. Raibert, *Legged robots that balance*. MIT press, 1986.
- [29] S. Rezazadeh, C. Hubicki, M. Jones, A. Peekema, J. Van Why, A. Abate, and J. Hurst, "Spring-mass walking with Atrias in 3D: Robust gait control spanning zero to 4.3 kph on a heavily underactuated bipedal robot," in *Dynamic Systems and Control Conference*, vol. 57243. American Society of Mechanical Engineers, 2015, p. V001T04A003.
- [30] Y. Guo, M. Zhang, H. Dong, and M. Zhao, "Fast online planning for bipedal locomotion via centroidal model predictive gait synthesis," *IEEE Robotics and Automation Letters*, vol. 6, no. 4, pp. 6450–6457, 2021.
- [31] X. Xiong and A. D. Ames, "Orbit characterization, stabilization and composition on 3D underactuated bipedal walking via hybrid passive linear inverted pendulum model," in *2019 IEEE/RSJ International Conference on Intelligent Robots and Systems (IROS)*. IEEE, 2019, pp. 4644–4651.
- [32] M. L. Felis, "Rbd: an efficient rigid-body dynamics library using recursive algorithms," *Autonomous Robots*, vol. 41, no. 2, pp. 495–511, 2017.
- [33] H. J. Ferreau, C. Kirches, A. Potschka, H. G. Bock, and M. Diehl, "qpoc: A parametric active-set algorithm for quadratic programming," *Mathematical Programming Computation*, vol. 6, no. 4, pp. 327–363, 2014.